minerals

MDPI

Article

Paleozoic Tectonothermal Evolution in the West Qinling Orogen, Central China: Petrological and Chronological Evidence from Garnet Amphibolites

Qi Guo [1,2], Xiaohong Mao [1,*], Jianxin Zhang [1] and Yawei Wu [1,2]

1 Key Laboratory of Deep-Earth Dynamics, Ministry of Natural Resources, Institute of Geology, Chinese Academy of Geological Sciences, Beijing 100037, China; qiguo716@stu.pku.edu.cn (Q.G.); zjx66@yeah.net (J.Z.); wuyawei@stu.pku.edu.cn (Y.W.)
2 School of Earth and Space Sciences, Peking University, Beijing 100871, China
* Correspondence: mxhcj40241055@163.com

Abstract: The Qinling Complex is located in the core of the northern Qinling Orogen and plays a key role in understanding the tectonic evolution of the Qinling Orogen, but its metamorphic evolution remains controversial. The combined investigation of petrographic observation, zircon U-Pb dating, and phase equilibria modeling for garnet amphibolites from the Tianshui area in the West Qinling Orogen is reported in this study. The results show that the garnet amphibolites record a clockwise *P-T* path characterized by a pre-T_{Max} decompression heating stage, a temperature peak at *P-T* conditions of 0.84–0.99 GPa and 869–886 °C, followed by a decompression cooling stage. Zircon U-Pb dating yields four age populations of ~479 ± 4 Ma, ~451 ± 8 Ma, ~411 ± 4 Ma, and ~377 ± 6 Ma. The 479–450 Ma reflects the timing of the pre-T_{Max} high–medium pressure upper amphibolite-facies metamorphism. The metamorphism at peak temperature condition occurred at *c*.411 Ma and was followed by decompression cooling to *c*.377 Ma. The Ordovician high–medium pressure metamorphism is related to the continental collision, which is slightly later than the HP–UHP eclogite-facies metamorphism in the East Qinling Orogen. The HT granulite-facies metamorphism at peak temperature condition took place at reduced pressures, suggesting thinning of the collision-thickened orogenic crust. Therefore, the northern West Qinling Orogen experienced a tectonothermal evolution from initial crust thickening to thinning during the Paleozoic collisional orogeny.

Keywords: West Qinling Orogen; garnet amphibolites; phase equilibria; zircon U-Pb dating; tectonothermal evolution

check for updates

Citation: Guo, Q.; Mao, X.; Zhang, J.; Wu, Y. Paleozoic Tectonothermal Evolution in the West Qinling Orogen, Central China: Petrological and Chronological Evidence from Garnet Amphibolites. *Minerals* **2023**, *13*, 1183. https://doi.org/10.3390/min13091183

Academic Editor: Jim Lee

Received: 4 July 2023
Revised: 25 August 2023
Accepted: 30 August 2023
Published: 8 September 2023

Copyright: © 2023 by the authors. Licensee MDPI, Basel, Switzerland. This article is an open access article distributed under the terms and conditions of the Creative Commons Attribution (CC BY) license (https://creativecommons.org/licenses/by/4.0/).

1. Introduction

Metamorphic rocks exposed in the orogen have been regarded as recording significant evidence of variation in pressure (*P*) and temperature (*T*), which represents the process of heating and cooling during burial, extension, and exhumation in particular tectonic settings, and the evidence of change in pressure and temperature can derive from the variation of mineral assemblages and compositions [1–10]. Especially, the ultrahigh-high to high pressure (UHP–HP) metamorphic rocks in orogen record a key evolution of transformation in the tectonic environment from subduction to continent–continent collision to collapse [9,11]. However, the mostly UHP–HP parageneses tend to be eliminated by decompression-induced partial melting or retrogression to form amphibolite-facies or (HP-) granulite-facies rocks [12–14]. Thus, determining the change of transient *P-T* conditions and constructing the *P-T* path of the metamorphic rocks are of fundamental importance in retrieving the tectonothermal evolution of the orogen [1–3,8,9].

High-grade metamorphic rocks are widely exposed in the northern part of the Qinling Orogen [15–17]. These metamorphic rocks were named the Qinling Complex (Group). However, their metamorphic evolution remains controversial. In the East Qinling Orogen, the Qinling Complex is mainly comprised of amphibolite-facies to granulite-facies gneisses with subordinate amounts of UHP–HP and ultrahigh-temperature (UHT) rocks [14–18]. Most studies suggest that the UHP–HP rock in the East Qinling Orogen formed in 500–485 Ma, representing the Cambrian continental deep subduction, whereas the widely distributed amphibolite-facies to granulite-facies rocks with clockwise *P-T* paths formed in 450–400 Ma, reflecting the collision and post-collision (overprint) event [14–22]. However, some authors suggested the Silurian high-temperature metamorphic event in the East Qinling Orogen formed in arc or arc-related tectonic environments which were related to the subduction of the Shangdan Ocean [23–29]. In particular, few studies have examined the Qinling Complex in the West Qinling Orogen. Recently, our studies showed that the metapelites and metamafic rocks from the Qinling Complex in Beidao and Huamiao areas of the West Qinling Orogen experienced 433–421 Ma granulite-facies metamorphism and 410–388 Ma retrograde metamorphism [30–32]. A garnet amphibolite records a ~497 Ma metamorphic event, which is interpreted as the eclogite-facies metamorphic age, based on it being a similar age to that of eclogites in the East Qinling Orogen [33], but no further petrological evidence supports this. Thus, a more detailed investigation on reconstructing the *P-T*-t path of metamorphic rock in the West Qinling Orogen is a key point in addressing the debates mentioned above.

The present study focuses on the petrology and geochronology of garnet amphibolites from the Qinling Complex of the West Qinling Orogen. We present an integrated study of mineral compositions, zircon U-Pb ages, and trace elements, as well as *P-T* conditions detected using phase equilibria modelling, for two representative garnet amphibolites. The results are used to construct their *P-T*-t paths, providing insights into the tectonothermal evolution from the thickening to thinning during collisional orogeny. Mineral abbreviations are from Whitney and Evans (2010) [34].

2. Geological Setting

The Qinling Orogen is separated from the North China Craton by the Linbao–Lushan–Wuyang fault (LLWF) to the north and from the Yangtze Craton by the Mianxian–Bashan–Xiangfan fault (MBXF) to the south. It is further divided into the North Qinling Orogen and South Qinling Orogen, which are separated by the Shangdan suture that resulted from the closure of the Paleozoic Shangdan Ocean [16,35,36]. The Qinling Orogen is also traditionally divided into West Qinling Orogen and East Qinling Orogen by Baoji-Chengdu Railway (Figure 1a,b).

In the eastern North Qinling Orogen (or northern East Qinling Orogen), four lithological units are recognized. They are the Kuanping Complex, Erlangping Complex, Qinling Complex, and Danfeng ophiolitic mélange from north to south [16]. The Qinling Complex mainly consists of high-grade metamorphic rocks including minor UHP eclogite and HP granulite, which is intruded by Paleozoic granitoid rocks. Their protoliths were formed during the Mesoproterozoic to early Neoproterozoic and underwent Early Paleozoic multistage metamorphism [18].

The present study area, located in the northern West Qinling Orogen, can be divided into three litho-tectonic units from north to south, including the Qingshui–Zhangjiachuan back-arc complex belt, Qinling arc metamorphic–magmatic complex belt, and Liziyuan subduction complex belt [30,31] (Figure 1c). Spatially, the latter two units correspond to the Qinling Complex and Danfeng ophiolitic mélange, whereas the former corresponds to the combination of the Kuanping Complex and Erlangping Complex in the northern East Qinling Orogen.

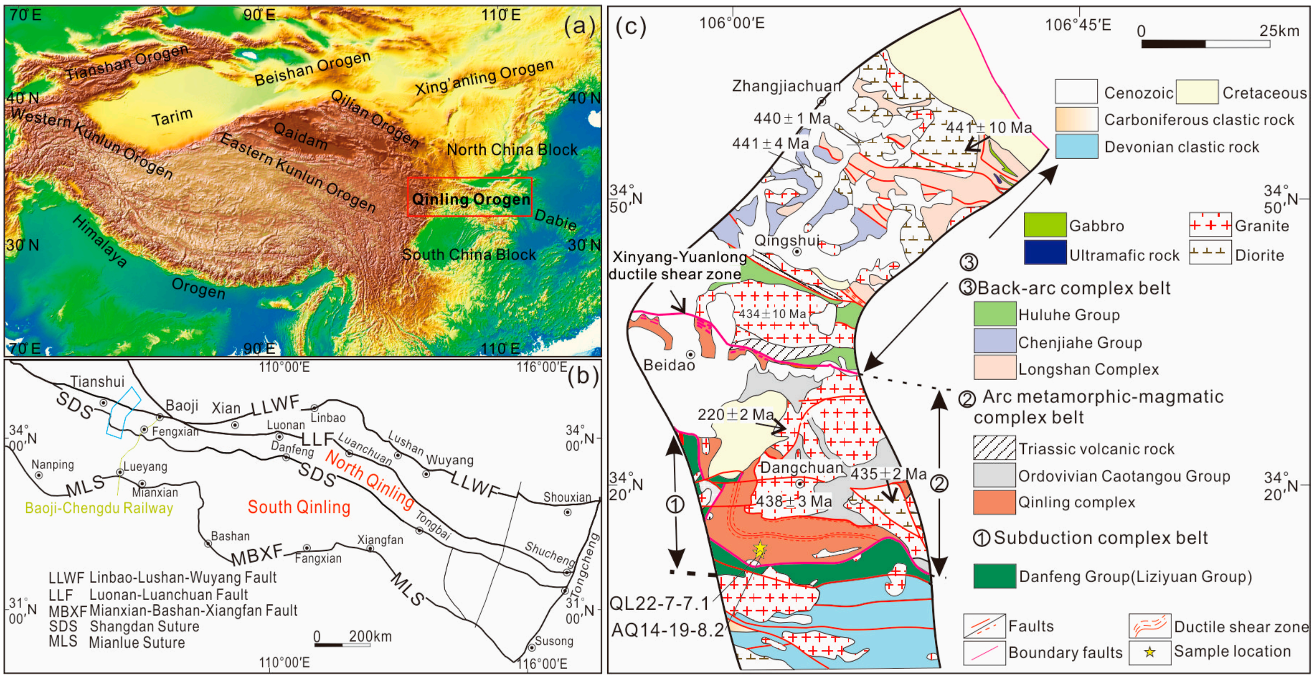

Figure 1. (**a**) Simplified tectonic location of the Qinling Orogen. (**b**) Simplified tectonic map of the Qinling orogen showing the location of the study area (modified after Dong et al. [15]). (**c**) Corridor-like geological sketch of the northern West Qinling Orogen (modified after Mao et al. [37]).

The Qingshui-Zhangjiachuan back-arc complex belt is bounded by the Xinyang–Yuanlong ductile shear zone on the south and covered by Quaternary sediments on the north. It consists mainly of the Huluhe Group, Hongtubao Formation, Chenjiahe Group, and Precambrian basement (Longshan Group), which is intruded by Paleozoic and Triassic intermediate and felsic intrusions exposed in the northern margin. The Huluhe Group is characterized by Ordovician–Silurian low-grade metamorphic clastic strata, including biotite-quartz schists, two-mica quartz schists, quartz phyllites, and quartzites [38]. The Late Cambrian–Early Silurian Hongtubao Formation is composed of basalt-basaltic andesite, volcanic rocks, and rare siliceous rocks, with lower greenschist-facies metamorphism [39]. The Ordovician Chenjiahe Group is mainly composed of andesitic and dacitic volcanic rocks, rhyolites, volcanic tuffs, sandstones, and terrigenous detrital rocks, which underwent lower greenschist-facies metamorphism [40]. The geochemical characteristics of the volcanic rocks in the Chenjiahe Group suggest an arc-related tectonic setting, similar to the Erlangping Group, which has been regarded as forming in the back-arc basin in the East Qinling Orogen [40,41].

The Qinling arc metamorphic–magmatic complex belt, which is located between the Xinyang–Yuanlong ductile shear zone and the Liziyuan subduction complex belt, mainly consists of the high-grade metamorphic Qinling Complex, Caotangou Group, and plutonic intrusions. The Qinling Complex is mainly composed of orthogneisses and paragneisses, which commonly enclose blocks of marbles and amphibolites. Most of these rocks underwent extensive migmatization, and some of them underwent Late Silurian granulite-facies metamorphism and anatexis [30,31]. The protolith age of orthogneisses is between 850 and 950 Ma [42,43]. The Caotangou Group is mainly composed of volcanic-clastic rocks and volcanic lava. The data reported previously indicates that some volcanic rocks in the Caotangou Group formed in a subduction-related arc environment in the late Ordovician [44,45]. The Dangchuan granitoid pluton, dated to approximately 438 Ma, has the feature of C-type adakitic rock, which is attributed to the partial melting of the thickened lower crust [46]. The Late Ordovician–Early Silurian Baihua magmatic complex, which is exposed at the east of the Qinling Complex (Figure 1c), exhibits a chemical resemblance to arc-related magma [47].

The Liziyuan subduction complex belt is sandwiched between the Qinling Complex and the Devonian Dacaotan Group. It is separated from the Qinling Complex to the north by a ductile shear zone and from the Dacaotan Group to the south by faults (Figure 1c). It mainly consists of metabasalt (greenschist and actinolite schist), sericite-bearing quartz schist, silty slate, arkose, andesitic porphyrite, and minor serpentinite, and underwent greenschist-facies and lower amphibolite-facies metamorphism. Geochemical data reveal that metabasalt has an affinity to N-MORB, representing part of the ocean ridge ophiolite [48]. Because of its close similarity to the Danfeng Group in the eastern North Qinling Orogen, the Liziyuan subduction complex belt has been considered part of the western extension of the Shangdan suture [16,17,48].

The samples for this study were collected from the Tianshui area. It is located in the Qinling arc metamorphic–magmatic complex belt (Figure 1c). At the outcrop scale, the garnet amphibolites occur as lenses surrounded by paragneisses (Figure 2). The garnet-bearing leucosomes occur as veins or boudins within migmatic paragneisses with widths from millimeters to centimeters and parallel to the foliations. Their patchy shape implies intensive ductile deformation (Figure 2).

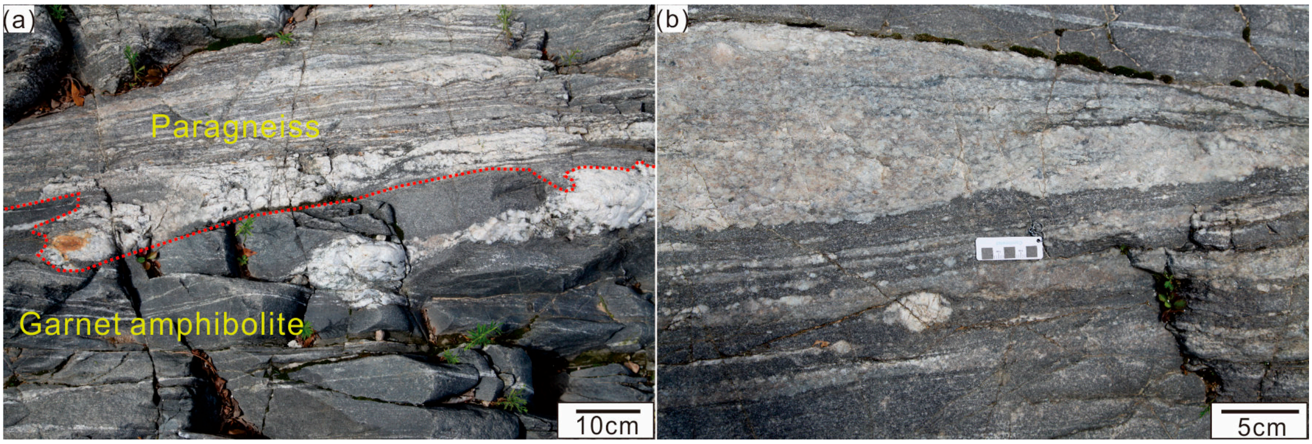

Figure 2. Photographs showing field occurrences of garnet amphibolites. (**a**) The boundary between garnet amphibolite and paragneiss. (**b**) The leucosomes occur as veins or boudins within magmatic paragneiss.

3. Analytical Methods

The bulk-rock composition was analyzed at the Wuhan Sample Solution Analytical Technology Co., Ltd., Wuhan, China. The major element was determined via X-ray fluorescence (XRF) and the analytical relative standard deviation is generally better than 2%. The chemical compositions of major minerals were obtained with a JEOL JXA-8100 electron microprobe at the Laboratory of the Continental Dynamics, Institute of Geology, Chinese Academy of Geological Sciences, Beijing, using a 15 kV accelerating voltage 20 nA beam current, 5 µm probe diameter (1–2 µm for some little mineral inclusions), and count times of 10 s for peak and 5 s for background per element; natural minerals were used for standardization, and ZAF corrections were carried out. The estimated precisions for major elements are ±2%. Mineral-phase scanning of thin sections was conducted with a TESCAN Integrated Mineral Analyser (TIMA) at the Laboratory of the Continental Dynamics, Institute of Geology, Chinese Academy of Geological Sciences, Beijing, using a beam current of 8.22 nA, a beam energy of 25 kV, and a working distance of 15 mm.

Zircon U-Pb analyses were conducted via LA-MC-ICP-MS at Beijing GeoAnalysis Co., Ltd. (Beijing, China). The analysis was performed with spot sizes of 30 µm at 6 Hz and a fluence of 5 J/cm^2. Pre-ablation was conducted for each spot analysis using 5 laser shots (~0.3 µm in depth) to remove potential surface contamination. Zircon Gj1 and 91500 were used as external standards for U-Pb isotope analysis. 91500, GJ-1, and Plesovice were analyzed twice every 10 analyses. NIST 610 and ^{91}Zr were used to calibrate the trace element concentrations as external and internal standard elements, respectively. Typically, 45 s of the sample signals were acquired after 25 s of gas background measurement. The exponential function was used to calibrate the downhole fractionation [49]. The Iolite software package (version 4) was used for data reduction [49]. The results of LA-ICP-MS U-Pb dating for separated zircons are listed in Supplementary Tables S1 and S2.

4. Result

4.1. Petrography and Mineral Chemistry

Garnet amphibolite samples in this study were collected from different outcrops in the Qinling Complex. The two representative garnet amphibolites have similar petrography and mineral assemblage. They are mainly composed of garnet (20%–25%), amphibole (30%–35%), and plagioclase (10%–15%), with varying amounts of clinopyroxene, K-feldspar, biotite, and quartz, and minor epidote, chlorite, titanite, rutile, ilmenite, sericite, and prehnite. Representative mineral compositions of garnet amphibolite samples are listed in Tables 1 and 2.

Table 1. Chemical composition of representative minerals from sample QL22-7-7.1.

Mineral	Grt			Amp			Cpx	
	Grt-C	**Grt-M**	**Grt-R**	**Amp-m**	**Amp-i-G**	**Amp-G-R**	**Cpx-m**	**Cpx-m**
SiO_2	37.23	37.02	37.09	42.47	42.38	43.18	50.45	50.98
TiO_2	0.03	0.04	0	1.89	1.56	1.46	0.08	0.10
Al_2O_3	20.79	20.82	20.62	10.91	11.01	10.62	0.49	0.95
Cr_2O_3	0.04	0.02	0.02	0.00	0.04	0.05	0.00	0.01
FeO	29.42	28.97	29.42	19.96	20.49	20.20	14.34	16.33
MnO	2.11	1.91	2.11	0.17	0.14	0.17	0.29	0.33
MgO	2.70	2.93	2.65	7.53	7.73	7.72	9.70	9.47
CaO	7.23	7.78	7.55	11.74	12.09	12.15	23.55	20.69
Na_2O	0.00	0.02	0.02	1.06	0.93	0.96	0.09	0.14
K_2O	0.00	0.00	0.00	1.22	1.23	1.18	0.00	0.01
Totals	99.55	99.52	99.47	96.95	97.59	97.68	98.99	99.01
O	12	12	12	23	23	23	6	6
Si	2.98	2.96	2.97	6.52	6.46	6.58	1.96	1.98
Ti	0.00	0.00	0.00	0.22	0.18	0.17	0.00	0.00
Al	1.96	1.96	1.95	1.98	1.98	1.91	0.02	0.04
Cr	0.00	0.00	0.00	0.00	0.01	0.01	0.00	0.00
Fe^{3+}	0.07	0.13	0.11	0.08	0.25	0.10	0.07	0.00
Fe^{2+}	1.90	1.81	1.86	2.48	2.36	2.47	0.40	0.53
Mn	0.14	0.13	0.14	0.02	0.02	0.02	0.01	0.01
Mg	0.32	0.35	0.32	1.72	1.76	1.75	0.56	0.55
Ca	0.62	0.67	0.65	1.93	1.98	1.98	0.98	0.86
Na	0.00	0.00	0.00	0.32	0.28	0.28	0.01	0.01
K	0.00	0.00	0.00	0.24	0.24	0.23	0.00	0.00
Sum	8.00	8.00	8.00	15.51	15.50	15.50	4.00	4.00
X(phase)	0.11	0.12	0.11	0.11	0.09	0.09	0.59	0.51
Y(phase)	0.22	0.24	0.23	0.41	0.43	0.41	0.00	0.01

Notes: X(Grt) = $Mg/(Mg + Ca + Fe^{2+})$; Y(Grt) = $Ca/(Mg + Ca + Fe^{2+})$; X(Amp) = Ti/2; Y(Amp)= $Mg/(Mg + Fe^{2+})$; X(Cpx) = $Mg/(Fe^{2+} + Mg)$; Y(Cpx) = $(2*Na/(2*Na + Ca + Mg + Fe^{2+})*Al/(Al + Fe^{3+}))$. -C, -M and -R refer to the core, mantle, and rim of garnet; -m refers to minerals occurring in matrix; -i-G refers to inclusion is included in garnet; -G-R refers to minerals occurring as a corona surrounding garnet.

Table 2. Chemical composition of representative minerals from sample AQ14-19-8.2.

Mineral	Grt			Amp			Pl	
	Grt-C	**Grt-M**	**Grt-R**	**Amp-m**	**Amp-i-G**	**Amp-G-R**	**Pl-m**	**Pl-G-R**
SiO_2	38.70	38.54	38.28	43.84	43.89	44.48	47.16	48.07
TiO_2	0.00	0.00	0.00	1.39	1.53	1.43	0.05	0.00
Al_2O_3	20.06	20.30	20.12	9.69	10.66	9.73	32.71	32.69
Cr_2O_3	0.00	0.00	0.00	0.00	0.01	0.06	0.01	0.04
FeO	27.21	27.41	28.93	18.87	18.79	17.85	0.15	0.18
MnO	2.64	2.45	2.39	0.22	0.22	0.18	0.00	0.00
MgO	3.50	3.54	3.04	9.61	8.81	9.94	0.04	0.25
CaO	6.96	7.00	6.80	11.79	11.14	11.99	18.13	16.65
Na_2O	0.00	0.02	0.00	1.05	1.13	1.02	1.18	1.22
K_2O	0.00	0.02	0.00	0.79	1.14	0.71	0.14	0.30
Totals	99.07	99.29	99.57	97.24	97.33	97.40	99.58	99.43
O	12	12	12	23	23	23	8	8
Si	3.09	3.07	3.06	6.41	6.62	6.67	2.18	2.21
Ti	0.00	0.00	0.00	0.22	0.17	0.16	0.00	0.00
Al	1.89	1.91	1.90	1.87	1.90	1.72	1.78	1.77
Cr	0.00	0.00	0.00	0.02	0.00	0.01	0.00	0.00
Fe^{3+}	0.00	0.00	0.00	0.60	0.24	0.27	0.01	0.01
Fe^{2+}	1.81	1.82	1.93	1.90	2.14	1.97	0.00	0.00
Mn	0.18	0.17	0.16	0.02	0.03	0.02	0.00	0.00
Mg	0.42	0.42	0.36	2.02	1.98	2.22	0.00	0.02
Ca	0.59	0.60	0.58	1.87	1.80	1.93	0.90	0.82
Na	0.00	0.00	0.00	0.28	0.33	0.30	0.11	0.11
K	0.00	0.00	0.00	0.12	0.22	0.14	0.01	0.02
Sum	7.97	7.98	7.99	15.33	15.42	15.39	4.98	4.96
X(phase)	0.15	0.15	0.13	0.11	0.09	0.08	0.89	0.87
Y(phase)	0.21	0.21	0.20	0.52	0.48	0.53		

Notes: X(Grt) = Mg/(Mg + Ca + Fe^{2+}); Y(Grt) = Ca/(Mg + Ca + Fe^{2+}); X(Amp) = Ti/2; Y(Amp) = Mg/(Mg + Fe^{2+}); X(Pl) = Ca/(Ca + Na + K). -C, -M and -R refer to the core, mantle and rim of garnet; -m refers to minerals occurring in matrix; -i-G refers to inclusion is included in garnet; -G-R refers to minerals occurring as a corona surrounding garnet.

Garnet generally occurs as anhedral and embayed porphyroblast with diameters of 0.5–2 mm. It is commonly surrounded by amphibole, plagioclase, and biotite, and contains inclusions of amphibole, quartz, rutile, ilmenite, plagioclase, and titanite. Multi-inclusions consisting of Pl + Qz ± Kfs are observed within a few garnet grains (Figure 3a–d,f–h). Amphibole mostly occurs as anhedral and subhedral grains in matrix, and some amphibole grains occur as inclusion within garnet porphyroblast or as coronae surrounding garnet (Figure 3a,b,f). Coarse-grained amphibole contains inclusions of garnet, ilmenite, plagioclase and clinopyroxene (Figure 3i,k,l), and the amphibole rims are partially replaced by the Chl + Prh + Ep (Figure 3a,k). Clinopyroxene occurs as matrix grains intergrowing with amphibole or as inclusions within the amphibole (Figure 3i–k). Clinopyroxene is partially replaced or surrounded by amphibole, suggesting a possible metamorphic reaction of Grt + Cpx → Amp + Pl (Figure 3j,l). A few clinopyroxenes occur as coronae with amphibole and plagioclase (Figure 3j). Plagioclase grains occur mainly as coronae surrounding garnet porphyroblast and in matrix; however, they are mostly replaced by sericite and prehnite (Figure 3a,c,f). A few plagioclase grains occur as part of multi-inclusions within garnet porphyroblast (Figure 3g). K-feldspar grains only occur as anhedral inclusions within garnet porphyroblasts or as cuspate films intergrowing with quartz along garnet boundaries (Figure 3c,h), suggesting an anatexis texture. Biotite occurs as fine-grained inclusions within ilmenite or grown around garnet porphyroblasts. Some biotite grains are completely replaced by chlorite and occur as pseudomorphs (Figure 3b,e). Ilmenite occurs as inclusions within amphibole and garnet or as anhedral coarse grains in the matrix (Figure 3a–c). Rutile only occurs as fine-grain inclusions within ilmenite (Figure 3d,e). Titanite mainly occurs as inclusions within the garnet core (Figure 3f).

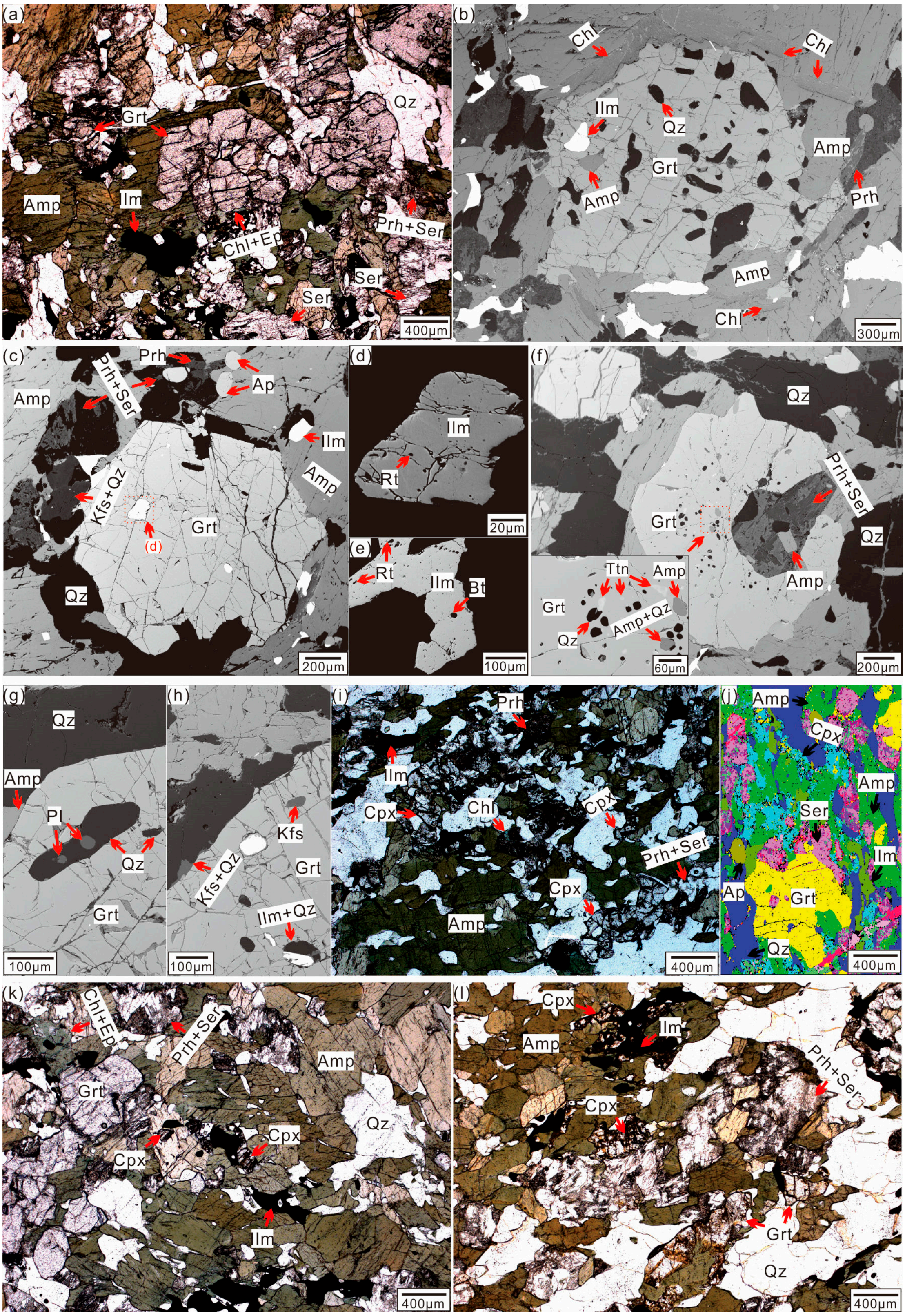

Figure 3. Photomicrographs image, TIMA mineral scanning map, and back-scattered image (BSE image) of the garnet amphibolites from the Tianshui area. (**a**) Amphibole, which is partly replaced by epidote + chlorite, occurs as corona surrounding relict garnet and plagioclase is completely replaced by prehnite + sericite assemblage. (**b**) Chlorite occurs as biotite pseudomorph in corona surrounding garnet. (**c**) Garnet rim is replaced by a corona of amphibole + prehnite + sericite + ilmenite + K-feldspar + quartz. (**d**) Fine-grained rutile is included in ilmenite. (**e**) Rutile and biotite are included in ilmenite.

(**f**) Titanite, amphibole, and multi-inclusion occur in the core of garnet. (**g**) Plagioclase is included in quartz, which is included in the mantle of garnet. (**h**) K-feldspar occurs as inclusion within the core–mantle transition of relict garnet and as cuspate film intergrown with quartz. (**i**) Clinopyroxene occurs in matrix and intergrown with amphibole; the garnet disappears in this texture domain. (**j**) Clinopyroxene occurs in corona and is replaced by amphibole. (**k**) Clinopyroxene occurs as inclusion within amphibole and amphibole is partly replaced by epidote + chlorite on the rim. (**l**) Garnet and clinopyroxene occur as relict grains in reaction texture and are almost replaced by amphibole.

Three generations of mineral assemblage can be identified based on the textural relations described above. The first generation (M1) is represented by inclusions of amphibole, K-feldspar, titanite, rutile, and quartz within garnet (core) and biotite inclusion within ilmenite (Figure 3c–h). The second generation (M2) is characterized by the mantle of garnet porphyroblast + coarse-grained amphibole + clinopyroxene (in the matrix or inclusion in amphibole) + plagioclase (in the matrix, but almost completely replaced by sericite and prehnite) + ilmenite + quartz (Figure 3a,c,k). The third generation (M3) is marked by the growth of corona around garnet porphyroblast and the disappearance of garnet, with an assemblage of Amp + Bt + Cpx + Pl + Ilm + Qz (Figure 3b,i,j,l).

Garnet has X_{Prp} (=Mg/(Mg + Fe^{2+} + Ca + Mn) of 0.10–0.12, X_{Alm} (=Fe^{2+}/(Mg + Fe^{2+} + Ca + Mn) of 0.61–0.64, X_{Grs}(=Ca/(Mg + Fe^{2+} + Ca + Mn) of 0.21–0.23, and X_{Sps} (=Fe^{2+}/(Mg + Fe^{2+} + Ca + Mn) of 0.04–0.05 in sample QL22-7-7.1 (Figure 4a) and X_{Prp} (=Mg/(Mg + Fe^{2+} + Ca + Mn) of 0.11–0.14, X_{Alm} (=Fe^{2+}/(Mg + Fe^{2+} + Ca + Mn) of 0.60–0.65, X_{Grs} (=Ca/(Mg + Fe^{2+} + Ca + Mn) of 0.19–0.20, and X_{Sps} (=Fe^{2+}/(Mg + Fe^{2+} + Ca + Mn) of 0.05–0.06 in sample AQ14-19-8.2 (Figure 4b). No obvious zoning is observed in the garnet core and mantle except for a significant increase in X_{Alm} and decrease in X_{Prp}, in the outermost rim.

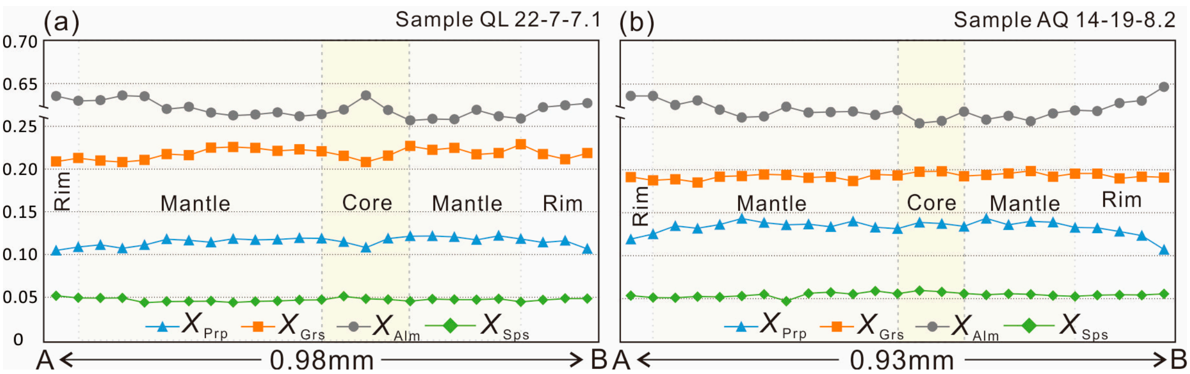

Figure 4. Representative composition zoning profiles of garnet from garnet amphibolites. (**a**) Garnet occurs in sample QL22-7-7.1. (**b**) Garnet occurs in sample AQ14-19-8.2.

The amphibole in the matrix exhibits compositional zoning with increasing Ti content from the core towards the mantle and decreasing Ti content from the mantle to rim (Figure 5a). It mainly has a ferro-hornblende and edenite composition with Ti content of 0.11–0.22 p.f.u., $Mg^{\#}$(=Mg/(Mg + Fe^{2+})) of 0.40–0.45, and Si content of 6.45–6.82 p.f.u. for sample QL22-7-7.1 and Ti of 0.11–0.22 p.f.u., $Mg^{\#}$ of 0.23–0.57, and Si of 6.21–6.96 p.f.u. for sample AQ14-19-8.2. The fine-grained amphibole within garnet mainly has a ferro-hornblende and magnesio-hornblende composition with Ti of 0.11–0.18 p.f.u., $Mg^{\#}$ of 0.43–0.58, and Si of 6.5–6.9 p.f.u. for sample QL22-7-7.1 and Ti of 0.11–0.18 p.f.u., $Mg^{\#}$ of 0.48–0.54, and Si of 6.4–6.8 p.f.u. for sample AQ14-19-8.2. The amphibole as coronae of garnet mainly has a ferro-hornblende and ferro-edenite composition with Ti of 0.10–0.18 p.f.u., $Mg^{\#}$ of 0.35–0.46, and Si of 6.07–6.74 p.f.u. for sample QL22-7-7.1 and Ti of 0.10–0.19 p.f.u., $Mg^{\#}$ of 0.43–0, 54 and Si of 6.35–6.83 p.f.u. for sample AQ14-19-8.2 (Figures 5b and 6).

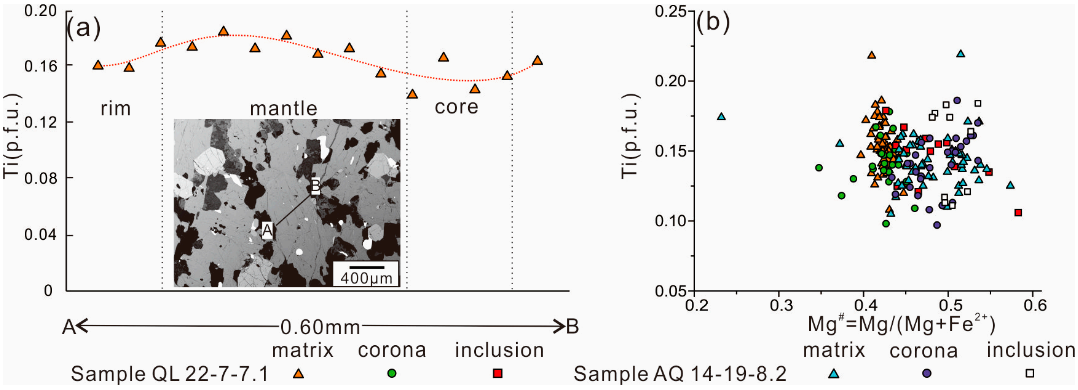

Figure 5. (**a**) Diagram for composition zoning of the representative amphibole. (**b**) Ti (p.f.u.) versus $Mg^{\#}$(=Mg/(Mg + Fe^{2+})) diagrams for the amphibole.

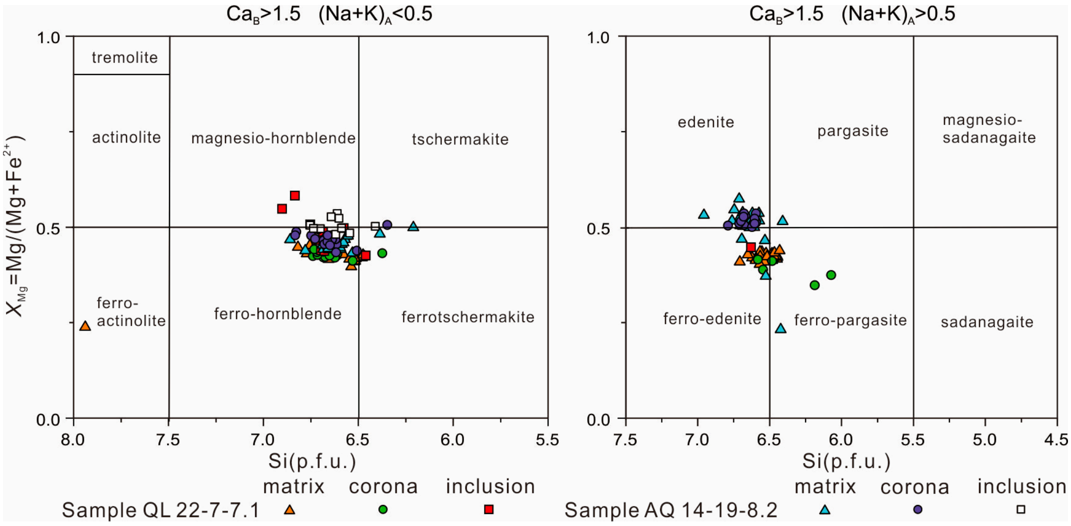

Figure 6. Diagram for classification of amphibole from garnet amphibolites [50].

Clinopyroxene shows a diopside or augite composition, with an X_{Mg}(=Mg/(Mg + Fe^{2+}) of 0.51–0.59 and a negligible X_{Jd} (=2*Na/(2*Na + Ca + Mg + Fe^{2+}) *Al/(Al + Fe^{3+})) of 0.001–0.012 (Figure 7a).

Plagioclase in the matrix of the sample AQ14-19-8.2 has an X_{An} of 0.84–0.99, and 0.87–0.91 in coronae (Figure 7b).

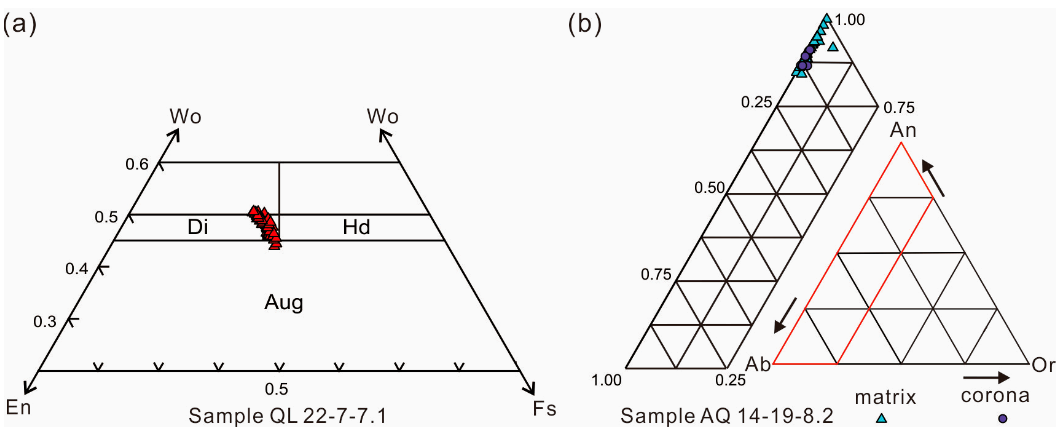

Figure 7. Diagram for classification of mineral. (**a**) Diagram for classification of clinopyroxene. (**b**) Ab-An-Or diagram of plagioclase.

4.2. Phase Equilibria Modeling

P-*T* pseudosections were calculated in NCKFMASHTO (Na_2O-CaO-K_2O-FeO-MgO-Al_2O_3-SiO_2-H_2O-TiO_2-O(Fe_2O_3)). The calculations were performed using the software GeoPs (version 3.4.8566.2826) [51] with the internally consistent thermodynamic dataset ds62 [52]. Activity–composition relationships were updated from those presented in Green et al. [53], which partial melting equilibria to be calculated for metabasic rocks. The fluid phase is considered to be pure H_2O. The determination of O (Fe_2O_3) and H_2O content is based on the T-M_O/T-M_{H_2O} diagram, ensuring that the final assemblages are stable near the solidus. The quartz, rutile, and titanite are regarded as pure endmember phases. P_2O_5 is disregarded as it mostly enters accessory apatite, and CaO accounting for apatite was subtracted from the bulk-rock compositions, whereas MnO was neglected in the calculations because of its limited effect in the amphibolite-facies to granulite-facies transition and mostly preserved in garnet.

The pseudosections were modelled with the measured bulk-rock composition, normalized on the basis of mole percent as follows: SiO_2 = 52.76, Al_2O_3 = 8.36, CaO = 9.16, MgO = 7.52, FeO = 13.74, K_2O = 1.04, Na_2O = 0.83, TiO_2 = 1.86, O = 1.34, and H_2O = 4.06 for sample QL22-7-7.1 and SiO_2 = 54.36, Al_2O_3 = 8.56, CaO = 9.14, MgO = 8.67, FeO = 11.24, K_2O = 0.86, Na_2O = 0.79, TiO_2 = 1.82, O =1.04, and H_2O = 4.03 for sample AQ14-19-8.2.

A *P*-*T* pseudosection was calculated for sample QL22-7-7.1 over a *P*-*T* window of 0.2–1.2 GPa and 600–1000 °C (Figure 8). The fluid-absent solidus lies between 675–747 °C, the garnet-out curve occurs at P = 0.36–0.77 GPa, the rutile-out curve occurs at P = 0.70–1.12 GPa, the ilmenite-out curve occurs at P = 0.70–1.20 GPa, the titanite-in curve occurs at T < 802 °C, and the biotite-out curve occurs at T = 780–832 °C. The *P*-*T* pseudosection is presented with the isopleths of X_{Prp} and X_{Grs} in garnet, X_{Ti} (=Ti/2) in amphibole, and the isopleths of X_{Mg} in clinopyroxene for relevant mineral assemblages.

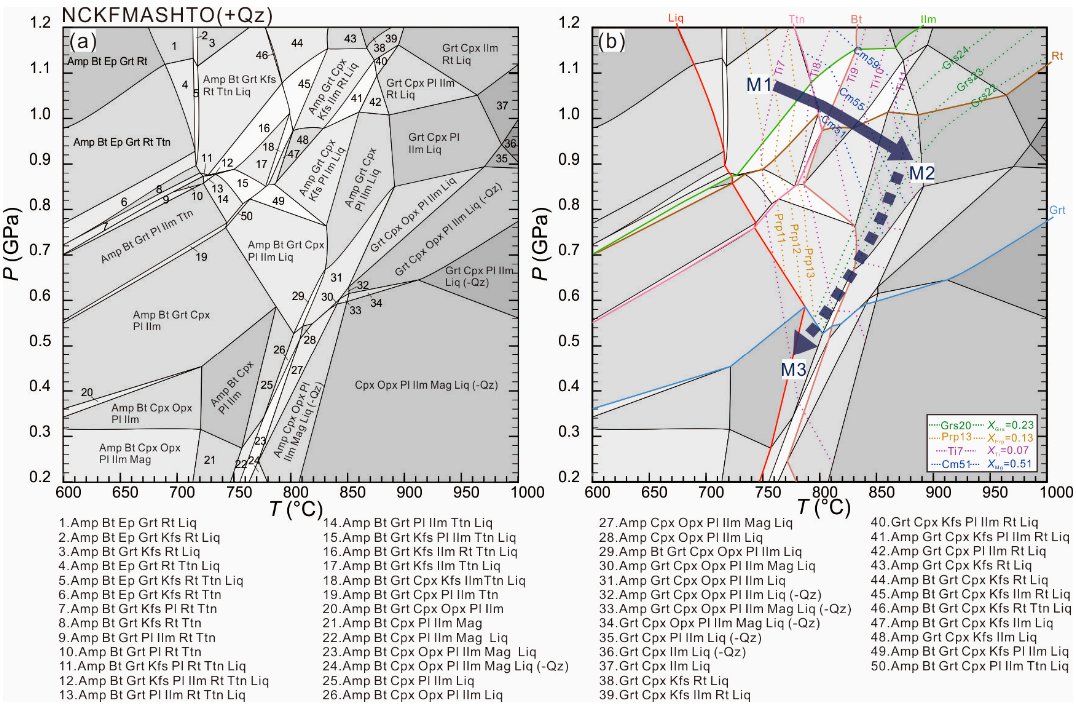

Figure 8. (**a**) *P*-*T* pseudosection calculated in the system NCKFMASHTO. (**b**) Estimated *P*-*T* path for garnet amphibolite sample (QL22-7-7.1). The pseudosection is contoured with isopleths of X_{Mg} = Mg/(Mg + Fe^{2+}) in clinopyroxene, X_{Ti} = (Ti/2) in amphibole, X_{Prp} (=Mg/(Mg + Fe^{2+} + Ca)), and X_{Grs} (=Ca/(Mg + Fe^{2+} + Ca)) in garnet. The colored full thick lines represent the position of the appearance or disappearance of minerals: the red full thick line represents the position of the solidus; the colored dash lines represent mineral compositional isopleths; the purple thick line with arrow represents the inferred *P*-*T* path.

The inferred M1 assemblage of Amp + Bt + Grt + Kfs + Rt + Ttn + Qz, and X_{Ti} isopleth in amphibole inclusion and the average X_{Prp} isopleth of garnet core constrain a *P-T* condition of ~1.08 GPa and 760 °C. The peak M2 assemblage of Amp + Grt + Cpx + Pl + Ilm + Qz + Liq is predicted to be stable in the *P-T* range of 0.67–1.02 GPa and 831–892 °C. The intersection of the isopleths for X_{Grs} in garnet, the highest X_{Ti} in amphibole, and the maximum X_{Mg} in clinopyroxene constrain the peak *P-T* conditions to 0.88–0.99 GPa and 869–886 °C. Meanwhile, the chemical composition isopleths in the peak assemblage stability field show different characteristics: the isopleths of X_{Grs} exhibit a positive slope with the X_{Grs} decreasing as temperature rises, the isopleths for X_{Mg} exhibit a relative steep negative slope with X_{Mg} increasing as pressure and temperature rise, and the isopleths of X_{Ti} show a steep negative slope with the X_{Ti} increasing as temperature rises. The retrograde M3 assemblage of Amp + Cpx + Bt + Pl + Ilm + Qz + Liq is predicted to be stable in the *P-T* range of 0.27–0.58 GPa and 757–802 °C; the disappearance of garnet is consistent with the formation of amphibole by consuming garnet and clinopyroxene that inferred from the variation of mineral amount modeled (Supplementary Figure S1).

A *P-T* pseudosection was calculated for sample AQ14-19-8.2 over a *P-T* window of 0.2–1.2 GPa and 600–1000 °C (Figure 9). The fluid-absent solidus lies between 691~750 °C and the pressure of H_2O-saturated solidus occurs under 0.28 GPa. The garnet-out curve occurs at P = 0.39–0.85 GPa, the rutile-out curve occurs at P = 0.63–0.95 GPa, the ilmenite-out curve occurs at P = 0.64–1.08 GPa, the titanite-in curve occurs at T < 805 °C, and the biotite-out curve occurs at T = 770–827 °C. The pseudosection is contoured with the isopleths of X_{Prp} and X_{Grs} for garnet, the isopleths of X_{Ti} for amphibole, and the isopleths of X_{An} for plagioclase.

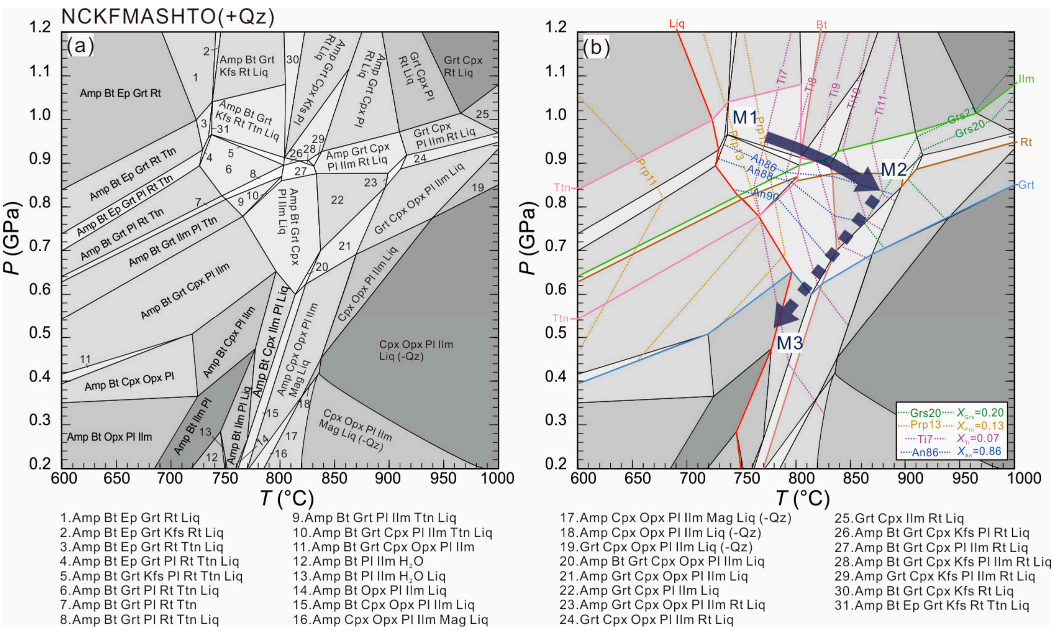

Figure 9. (**a**) *P-T* pseudosection calculated in the system NCKFMASHTO. (**b**) Estimated *P-T* path for garnet amphibolite (sample AQ14-19-8.2). The pseudosection is contoured with isopleths of X_{An}= Ca/(Ca + Na + K) in plagioclase, X_{Ti} = (Ti/2) in amphibole, X_{Prp}(=Mg/(Mg + Fe^{2+} + Ca)) and X_{Grs}(=Ca/(Mg + Fe^{2+} + Ca)) in garnet. The colored full thick lines represent the position of the appearance or disappearance of minerals; the red full thick line represents the position of the solidus; the colored dash lines represent mineral compositional isopleths; the purple thick line with arrow represents the inferred *P-T* path.

The inferred M1 assemblage of Amp + Bt + Grt + Kfs + Rt +Ttn + Qz, and X_{Ti} isopleth in amphibole inclusion, and the average X_{Prp} isopleth of the garnet core constrain a *P-T* condition of ~0.95 GPa and ~770 °C. The peak M2 assemblage of Amp + Grt + Cpx + Pl + Ilm + Qz + Liq is predicted to be stable in a *P-T* range of 0.70–0.88 GPa and 838–899 °C.

The intersection of isopleths for X_{Grs} of 0.21 and the highest X_{Ti} of 0.11 reveal that the peak *P-T* condition is at conditions of 0.84 Gpa and 880 °C. The M3 assemblage of Amp + Cpx + Bt + Pl + Ilm + Qz + Liq is predicted to be stable in the *P-T* range of 0.27–0.65 GPa and 771–812 °C.

4.3. Zircon U-Pb Chronology

Zircon separated from sample QL22-7-7.1 are 30–150 μm long with aspect ratios of 1.0–3.5. Most zircon grains are round to weakly elongated in shape, with a bright core and dark-grey rim in CL images. A few grains are completely dark-grey or nearly black. The cores of zircon are homogeneous or show weak sector zoning, and the rims exhibit nebulous or patchy zoning (Figure 10).

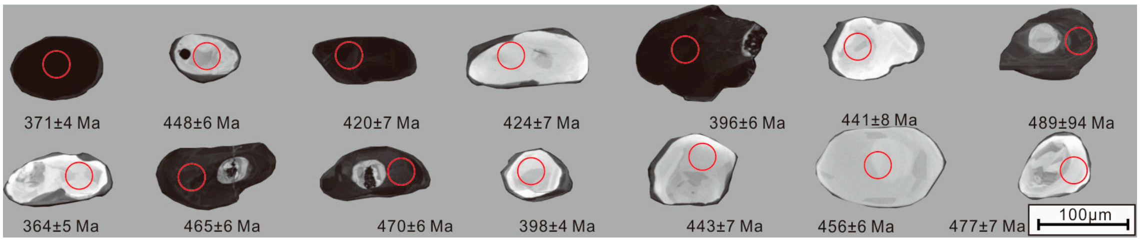

Figure 10. Representative cathodoluminescence (CL) images of zircons from a garnet amphibolite, showing the analyzed spot and relevant ages.

A total of 50 spots were analyzed. Excluding 10 discordant analyses, the remaining 40 analyses yielded $^{206}Pb/^{238}U$ age between 364 Ma and 517 Ma. These analyses can be divided into four age populations, and yield weighted mean ages of ~377 ± 6 Ma (MSWD = 3.8; n = 11), ~411 ± 4 Ma (MSWD = 4.4; n = 20), ~451 ± 8 Ma (MSWD = 1.4; n = 6), and ~479 ± 4 Ma (MSWD = 0.32; n = 3), respectively (Figure 11a). There are two types of chondrite-normalized rare earth element (REE) patterns of zircons; some zircons show characteristic of steep heavy rare earth element (HREE) slopes and the majority of these zircons are in the ~377 Ma age cluster, while the others show relatively flat HREE slopes and are mainly in another three age clusters (Figure 11b). The zircons show slightly positive or no Eu anomaly, which mainly suggests the age of ~479 Ma and ~451 Ma clusters (δEu = 1.02–1.27), representing zircon growth under a condition of the absence of plagioclase; the zircons displaying slightly to obviously negative Eu anomalies mainly suggest the ~411 Ma and ~377 Ma age clusters.

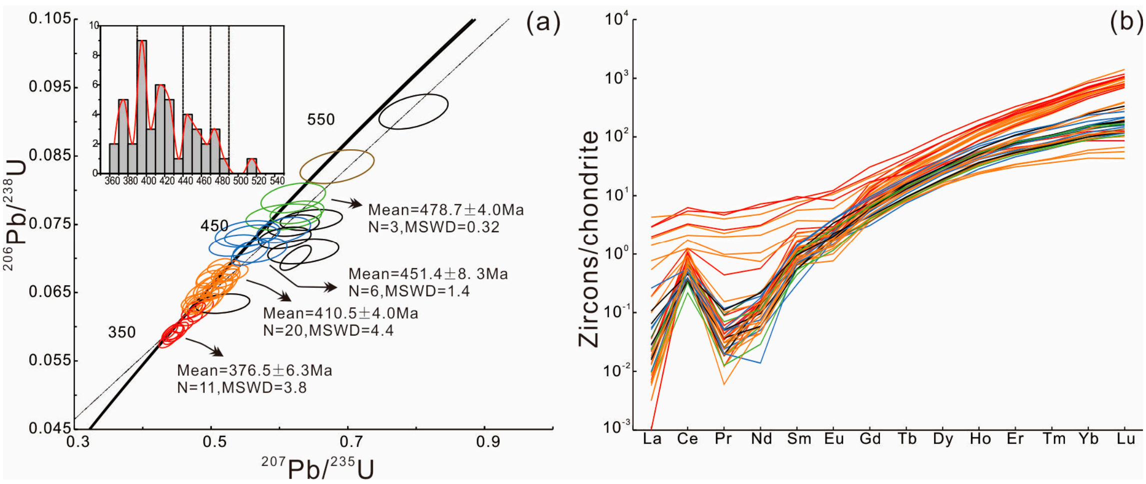

Figure 11. (**a**) U-Pb concordia diagram of zircon with the statistical histogram of relevant age. (**b**) Chondrite-normalized REE patterns of zircons. (Chondrite normalization uses values from Sun and McDonough [54].

5. Discussion

5.1. Metamorphic Evolution

Our comprehensive study involving petrographic observations, mineral compositions, and phase equilibria modeling suggests two stages of metamorphic evolution for garnet amphibolites from the West Qinling Orogen: a pre-T_{Max} decompression heating stage and a post-T_{Max} decompression cooling (Figures 8 and 9). No evidences of HP–UHP metamorphism were identified through petrologic observation and pseudosection, although a few zircons of 480–500 Ma may possibly have recorded an early metamorphic event related to eclogite-facies metamorphism, based on comparison with similar ages recorded in eclogites from the East Qinling Orogen ([33], this study, see discussion below). The M1 stage is based on the inclusion assemblage in garnet, and the *P-T* conditions are constrained to ~1.08 GPa and ~760 °C for sample QL22-7-7.1 and ~0.95 GPa and ~770 °C for sample AQ14-19-8.2, which, using X_{Ti} isopleth and X_{Prp} isopleth in amphibole inclusion and the core of garnet, reflect medium–high pressure upper amphibolite-facies to granulite-facies conditions, consistent with the inclusion assemblage of garnet + amphibole + biotite + K-feldspar + rutile + titanite + Qz (Figures 8 and 9).

The *P-T* conditions of the M2 stage are constrained to 0.88–0.99 GPa and 869–886 °C for sample QL22-7-7.1 and 0.84 GPa and 880 °C for sample AQ14-19-8.2, respectively, which are similar to granulite-facies conditions of 0.78–1.02 GPa and 770–820 °C reported previously in pelite granulite from the Qinling complex in the same area [31,32] (Figure 12). Therefore, a *P-T* vector with decreasing pressure and increasing temperature is preferred from the pre-peak to peak temperature stage. The slightly different peak *P-T* conditions detected from the two samples can be regarded as representing the different degrees of melt loss at suprasolidus conditions [55].

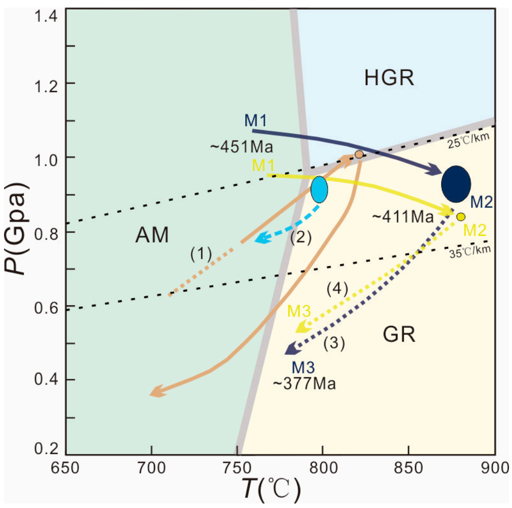

Figure 12. The *P-T* path deduced for high-grade metamorphic rocks from the northern West Qinling Orogen. The *P-T* paths are labeled as follows: (1) garnet-sillimanite-biotite gneiss from the Beidao area [32]; (2) paragneiss from the Huamiao area [31]; (3) garnet amphibolite of sample QL22-7-7.1 in this study; (4) garnet amphibolite of sample AQ14-19-8.2 in this study. Metamorphic facies boundaries are from Wei et al. [56]. Abbreviations: GR = granulite; AM = amphibolite; HGR = high-pressure granulite.

In the M3 stage, decompression cooling to fluid-absent solidus is recorded in the composition variation of clinopyroxene of sample QL22-7-7.1, the plagioclase of sample AQ14-19-8.2, and the amphibole in both samples. As two samples were collected from the same location, their post-peak paths should share identical pressures. However, the inferred post-T_{Max} decompression cooling paths show a slight difference. The cooling evolution at suprasolidus mainly occurs under conditions with melt-involved reactions.

This evolution may not occur in an equilibrium state at the solidus and may record diverse *P*-*T* condition along the cooling *P*-*T* path [55].

Generally, by integrating the metamorphic stages recorded in two garnet amphibolites, a clockwise *P*-*T* path with pre-T_{Max} decompression heating and post-T_{Max} decompression cooling can be defined.

5.2. Zircon U-Pb Age Interpretations

Zircon is one of the main minerals used in the geochronological age dating of high-grade metamorphic rocks and can grow at various stages of subsolidus prograde metamorphism and melt crystallization in retrograde metamorphism [57–59]. It has widely been considered to retain characteristics of trace elements extracted from effective bulk rock composition linked with major minerals like garnet and plagioclase as it is mechanically and chemically robust [60–64]. However, the decoupling of U-Pb ages and element abundances induced by the distortion of the crystal lattice and diffusion of elements at high temperatures has provided a challenge to the interpretation of ages obtained from zircon [65–70].

Our data from zircons in garnet amphibolite show a negative correlation for ∑HREE-ages and Y-ages, and a positive correlation for δEu-ages (Figure 13). Zircon U-Pb datings of sample QL22-7-7.1 yield four age clusters: *c*.479 ± 4 Ma, *c*.451 ± 8 Ma, *c*.411 ± 4 Ma, and *c*.377 ± 6 Ma. The 479 Ma and 451 Ma clusters display flat HREE patterns without obvious Eu anomalies, suggesting that they were formed in the presence of garnet but in the absence of plagioclase, which is commonly interpreted as eclogite-facies conditions. However, in this study, the plagioclase begins to appear during the decompression heating stage after medium–high pressure upper amphibolite-facies to granulite-facies metamorphism (Supplementary Figures S1 and S2). Therefore, the two age clusters should reflect the timings prior to the decompression heating stage. Combined with the previous investigations, which reported significant 485–518 Ma HP–UHP metamorphism in the Qinling Orogen [14–20], we infer that 451 ± 8 Ma may possibly date the timing of medium–high pressure upper amphibolite-facies to granulite-facies condition prior to decompression heating, and 479 ± 4 Ma possibly represents an earlier metamorphic age, even an eclogite-facies metamorphic age, although no corresponding eclogitic assemblage was recorded in the studied samples. Most zircons of the 411 Ma cluster display flat HREE patterns with slight Eu anomalies, suggesting that they were formed in presence of garnet and plagioclase, consistent with the constant modal amounts of garnet and appearance of small modal amounts of plagioclase along the decompression heating *P*-*T* path (Supplementary Figures S1 and S2). Therefore, we explain 411 Ma as a time of near peak temperature conditions. Zircons of the 377 Ma cluster show steep HREE patterns with slight to obvious Eu negative anomalies and increasing Y content (Figures 11 and 13), suggesting the garnet breakdown and plagioclase growth during the decompression cooling stage (Supplementary Figures S1 and S2). Thus, we infer that 377 Ma represents the age of *P*-*T* vector approach to solidus during retrogression.

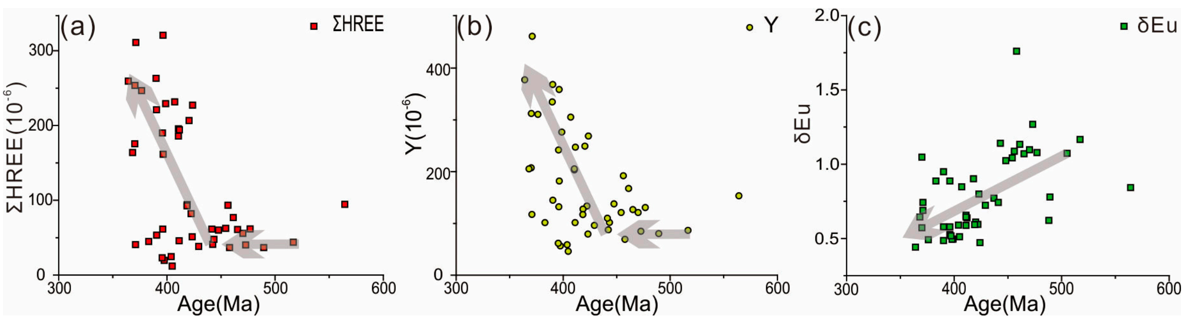

Figure 13. Diagrams of (**a**) ∑HREE vs. age, (**b**) Y vs. age, and (**c**) δEu vs. age of zircons.

5.3. Tectonic Implications

The West Qinling Orogen is commonly considered the western extension of the East Qinling Orogen, and both orogens contain similar, high-grade Qinling Complex [15–17,30–32]. However, Cambrian–early Ordovician HP–UHP metamorphic assemblage had not been detected, although the Cambrian age obtained recently from garnet amphibolite was interpreted as an eclogite-facies age similar to that in the East Qinling Orogen [33]. In this study, the 479–451 Ma age is suggested as dating the timing of medium–high pressure upper amphibolite-facies to granulite-facies metamorphism prior to peak temperature, indicating that the West Qinling Orogen experienced a crust thickening during the Ordovician collision orogeny, which resulted from the collision of the North Qinling microcontinent with the North China Craton [15–18,30–32]. Our results did not provide a record of Cambrian continental deep subduction, as that in the East Qinling Orogen [16–18,71,72]. One possibility is that garnet amphibolite in the West Qinling Orogen experienced a similar Cambrian HP–UHP metamorphism, but its metamorphic assemblage had been completely obscured by high-temperature overprint, except for the zircon dating record [33]. Another possibility is that the West Qinling Orogen did not experience a deep continental subduction, although a synchronous or slightly later collisional thickening also occurred. However, the present data are insufficient to distinguish between these two possibilities.

As shown by the *P*-*T*-t path presented in Figure 12, the garnet amphibolite in the West Qinling Orogen experienced a heating process during decompression and then attained high-temperature granulite-facies conditions at peak temperature. This indicates metamorphism at high thermal gradients in shallower crust levels. We suggest that the high-temperature granulite-facies metamorphism resulted from crustal extension after thickening related to the collision. The extension was commonly considered to be in response to lithospheric thinning related to asthenospheric upwelling [73,74]. Therefore, it is proposed that the West Qinling Orogen was thickened by continental collision in the late Cambrian–Ordovician and then thinned due to lithosphere extension in the late Silurian–Early Devonian. This situation is also reported in the East Qinling Orogen and Tongbai Orogen, although the time from compression to extension remains controversial [17,22,72,75]. Generally, we inferred that the whole Qinling Orogen experienced a Paleozoic orogenic process from the collision-related compression to post-collision extension.

6. Conclusions

(1) Garnet amphibolites from the Qinling Complex in the West Qinling Orogen recorded two metamorphic stages involving decompression heating prior to peak granulite-facies metamorphism (0.84–0.99 GPa and 869–886 °C), and followed by a stage of decompression cooling, suggesting a clockwise *P*-*T* path.

(2) The 479–450 Ma age reflects the timing of the high–medium upper amphibolite-facies metamorphism. The metamorphism at peak temperature condition occurred at *c*.410 Ma, followed by decompression cooling to *c*.377 Ma.

(3) The Ordovician high–medium pressure amphibolite-facies metamorphism was related to crustal thickening caused by continental collision. The HT granulite-facies metamorphism at peak temperature condition took place at reduced pressures, suggesting thinning of the collision-thickened orogenic crust. The West Qinling Orogeny experienced a tectonothermal evolution from initial crust thickening to thinning during the Paleozoic collisional orogeny.

Supplementary Materials: The following supporting information can be downloaded at: https://www.mdpi.com/article/10.3390/min13091183/s1, **Table S1**: Zircon U-Pb isotope data were obtained by LA-ICP-MS for sample QL22-7-7.1 ($\times 10^{-6}$). Table S2: LA-ICP-MS rare earth elements of zircon from QL22-7-7.1 ($\times 10^{-6}$). Figure S1: Modeled mineral proportions for the garnet amphibolite from sample QL22-7-7.1: (**a**) garnet; (**b**) clinopyroxene; (**c**) amphibole; (**d**) plagioclase. Figure S2: Modeled mineral proportions for the garnet amphibolite from sample AQ14-19-8.2: (**a**) garnet; (**b**) clinopyroxene; (**c**) amphibole; (**d**) plagioclase.

Author Contributions: Conceptualization, J.Z. and Q.G.; field survey and geological interpretation, J.Z. and X.M.; sample collection, J.Z., X.M., Q.G. and Y.W.; methodology, J.Z. and X.M.; investigation and data processing, Q.G.; writing—original draft preparation, Q.G.; writing—review and editing J.Z. and Q.G.; supervision, J.Z. and X.M. All authors have read and agreed to the published version of the manuscript.

Funding: This work was financially supported by (1) National Natural Science Foundation of China: 42202058; (2) National Natural Science Foundation of China: 42072237; (3) the Geological Survey Project of China: DD20221649.

Data Availability Statement: All data can be provided from Q.G. upon request.

Acknowledgments: We would like to thank Xin Dong for technical assistance in the TIMA scan. We appreciate thoughtful comments from three anonymous reviewers that improved the paper quality.

Conflicts of Interest: The authors declare no conflict of interest.

References

1. Miyashiro, A. Evolution of Metamorphic Belts. *J. Petrol.* **1961**, *2*, 277–311. [CrossRef]
2. England, P.C.; Thompson, A.B. Pressure-Temperature-Time Paths of Regional Metamorphism I. Heat-Transfer During the Evolution of Regions of Thickened Continental Crust. *J. Petrol.* **1984**, *25*, 894–928. [CrossRef]
3. Thompson, A.B.; England, P.C. Pressure-Temperature-Time Paths of Regional Metamorphism II. Their Inference and Interpretation using Mineral Assemblages in Metamorphic Rocks. *J. Petrol.* **1984**, *25*, 929–955. [CrossRef]
4. Harley, S.L. The origins of granulites: A metamorphic perspective. *Geol. Mag.* **1989**, *126*, 215–247. [CrossRef]
5. Sandiford, M.; Powell, R. Deep crustal metamorphism during continental extension: Modern and ancient examples. *Earth Planet. Sci. Lett.* **1986**, *79*, 151–158. [CrossRef]
6. Bohlen, S.R. Pressure-Temperature-Time Paths and a Tectonic Model for the Evolution of Granulites. *J. Geol.* **1987**, *95*, 617–632. [CrossRef]
7. Bohlen, S.R. On the formation of granulites. *J. Metamorph. Geol.* **1991**, *9*, 223–229. [CrossRef]
8. Brown, M. P-T-t evolution of orogenic belts and the causes of regional metamorphism. *J. Geol. Soc.* **1993**, *150*, 227–241. [CrossRef]
9. Brown, M.; Johnson, T. Time's arrow, time's cycle: Granulite metamorphism and geodynamics. *Mineral. Mag.* **2019**, *83*, 323–338. [CrossRef]
10. Holder, R.M.; Viete, D.R.; Brown, M.; Johnson, T.E. Metamorphism and the evolution of plate tectonics. *Nature* **2019**, *572*, 378–381. [CrossRef] [PubMed]
11. Zhang, L.; Wang, Y. The exhumation of high- and ultrahigh-pressure metamorphic terranes in subduction zone: Questions and discussions. *Sci. China Earth Sci.* **2020**, *63*, 1884–1903. [CrossRef]
12. Cheng, H.; Zhang, C.; Vervoort, J.D.; Li, X.; Li, Q.; Zheng, S.; Cao, D. Geochronology of the transition of eclogite to amphibolite facies metamorphism in the North Qinling orogen of central China. *Lithos* **2011**, *125*, 969–983. [CrossRef]
13. Keller, D.S.; Ague, J.J. Quartz, mica, and amphibole exsolution from majoritic garnet reveals ultra-deep sediment subduction, Appalachian orogen. *Sci. Adv.* **2020**, *6*, eaay5178. [CrossRef]
14. Liu, L.; Liao, X.; Zhang, C.; Chen, D.; Gong, X.; Kang, L. Multi-matemorphic timings of HP-UHP rocks in the North Qinling and their geological implications. *Acta Petrol. Sin.* **2013**, *29*, 1634–1656. (In Chinese)
15. Dong, Y.; Zhang, G.; Neubauer, F.; Liu, X.; Genser, J.; Hauzenberger, C. Tectonic evolution of the Qinling orogen, China: Review and synthesis. *J. Asian Earth Sci.* **2011**, *41*, 213–237. [CrossRef]
16. Dong, Y.; Santosh, M. Tectonic architecture and multiple orogeny of the Qinling Orogenic Belt, Central China. *Gondwana Res.* **2016**, *29*, 1–40. [CrossRef]
17. Liu, L.; Liao, X.; Wang, Y.; Wang, C.; Santosh, M.; Yang, M.; Zhang, C.; Chen, D. Early Paleozoic tectonic evolution of the North Qinling Orogenic Belt in Central China: Insights on continental deep subduction and multiphase exhumation. *Earth-Sci. Rev.* **2016**, *159*, 58–81. [CrossRef]
18. Zhang, J.; Yu, S.; Meng, F. Ployphase Early Paleozoic metamorphism in the northern Qinling orogenic belt. *Acta Petrol. Sin.* **2011**, *27*, 1179–1190. (In Chinese)
19. Bader, T.; Ratschbacher, L.; Franz, L.; Yang, Z.; Hofmann, M.; Linnemann, U.; Yuan, H. The heart of China revisited, I. Proterozoic tectonics of the Qin mountains in the core of supercontinent Rodinia. *Tectonics* **2013**, *32*, 661–687. [CrossRef]
20. Bader, T.; Franz, L.; Ratschbacher, L.; de Capitani, C.; Webb, A.A.G.; Yang, Z.; Pfander, J.A.; Hofmann, M.; Linnemann, U. The Heart of China revisited: II Early Paleozoic (ultra)high-pressure and (ultra)high-temperature metamorphic Qinling orogenic collage. *Tectonics* **2013**, *32*, 922–947. [CrossRef]
21. Bader, T.; Zhang, L.; Li, X.; Xia, B.; Franz, L.; Capitani, C.; Li, Q. High-P granulites of the Songshugou area (Qinling Orogen, east-central China): Petrography, phase relations, and U/Pb zircon geochronology. *J. Metamorph. Geol.* **2020**, *38*, 421–450. [CrossRef]

22. Ratschbacher, L.; Hacker, B.R.; Calvert, A.; Webb, L.E.; Grimmer, J.C.; McWilliams, M.O.; Ireland, T.; Dong, S.; Hu, J. Tectonics of the Qinling (Central China): Tectonostratigraphy, geochronology, and deformation history. *Tectonophysics* **2003**, *366*, 1–53. [CrossRef]
23. Wang, Z.; Yan, Q.; Yan, Z.; Wang, T.; Jiang, C.; Gao, L.; Li, Q.; Chen, J.; Zhang, Y.; Liu, P.; et al. New Division of the Main Tectonic Units of the Qinling Orogenic Belt, Central China. *Acta Geol. Sin.* **2009**, *83*, 1527–1546. (In Chinese)
24. Liu, X.; Jahn, B.M.; Hu, J.; Li, S.; Liu, X.; Song, B. Metamorphic patterns and SHRIMP zircon ages of medium-to-high grade rocks from the Tongbai orogen, central China: Implications for multiple accretion/collision processes prior to terminal continental collision. *J. Metamorph. Geol.* **2011**, *29*, 979–1002. [CrossRef]
25. Xiang, H.; Zhang, L.; Zhong, Z.; Santosh, M.; Zhou, H.; Zhang, H.; Zheng, J.; Zheng, S. Ultrahigh-temperature metamorphism and anticlockwise P-T–t path of Paleozoic granulites from north Qinling-Tongbai orogen, Central China. *Gondwana Res.* **2012**, *21*, 559–576. [CrossRef]
26. Xiang, H.; Zhang, Z.; Lei, H.; Qi, M.; Dong, X.; Wang, W.; Lin, Y. Paleoproterozoic ultrahigh-temperature pelitic granulites in the northern Sulu orogen: Constraints from petrology and geochronology. *Precambrian Res.* **2014**, *254*, 273–289. [CrossRef]
27. Xiang, H.; Zhang, Z.; Zhao, L.; Zhong, Z.; Zhou, H. Metamorphic P-T-t Path of UHT Granulites from the North Tongbai Orogen, Central China. *J. Earth Sci.* **2018**, *29*, 1116–1131. [CrossRef]
28. Wu, Y.; Zheng, Y. Southward accretion of the North China Block and the tectonic evolution of the Qinling-Tongbai-Hong'an orogenic belt. *Chin. Sci. Bull.* **2013**, *58*, 2246–2250. (In Chinese)
29. Xu, Z.; Li, Y.; Ji, S.; Li, G.; Pei, X.; Ma, X.; Xiang, H.; Wang, R. Qinling gneiss domes and implications for tectonic evolution of the Early Paleozoic Orogen in Central China. *J. Asian Earth Sci.* **2020**, *188*, 104052. [CrossRef]
30. Mao, X.; Zhang, J.; Yu, S.; Li, Y.; Yu, X.; Lu, Z. Early Paleozoic granulite-facies metamorphism and anatexis in the northern West Qinling orogen: Monazite and zircon U-Pb geochronological constraints. *Sci. China-Earth Sci.* **2017**, *60*, 943–957. [CrossRef]
31. Mao, X.; Zhang, J.; Yu, S.; Li, Y.; Yu, X.; Lu, Z.; Zhou, G. Metamorphism of Qinling Complex in Northern West Qinling Orogen: Petrology, Phase Equilibria Modelling of Paragneiss and Their Geological Implication. *Earth Sci.* **2018**, *43*, 278–295. (In Chinese)
32. Guo, Q.; Mao, X.; Zhang, J.; Lu, Z.; Zhou, G.; Teng, X.; Wu, Y. Granulite-facies metamorphism in the northern part of West Qinling: Constraints from phase equilibrium modeling and in-situ U-Pb dating of monazite. *Acta Petrol. Sin.* **2022**, *38*, 3259–3280. (In Chinese) [CrossRef]
33. Tang, Y.; Chen, D.; Ren, Y.; Wang, H. Discovery of Early Paleozoic eclogite-facies metamorphic rocks in the western part of North Qinling Orogen and its geological significance. *Acta Petrol. Sin.* **2022**, *38*, 585–597. (In Chinese) [CrossRef]
34. Whitney, D.L.; Evans, B.W. Abbreviations for names of rock-forming minerals. *Am. Mineral.* **2009**, *95*, 185–187. [CrossRef]
35. Meng, Q.; Zhang, G. Timing of collision of the North and South China blocks: Controversy and reconciliation. *Geology* **1999**, *27*, 123–126. [CrossRef]
36. Dong, Y.; Zhang, G.; Hauzenberger, C.; Neubauer, F.; Yang, Z.; Liu, X. Palaeozoic tectonics and evolutionary history of the Qinling orogen: Evidence from geochemistry and geochronology of ophiolite and related volcanic rocks. *Lithos* **2011**, *122*, 39–56. [CrossRef]
37. Mao, X.; Zhang, J.; Lu, Z.; Zhou, G.; Teng, X. Structural style and geochronology of ductile shear zones in the western north Qinling orogenic belt, Central China: Implications for Paleozoic orogeny in the Central China orogeny. *J. Asian Earth Sci.* **2020**, *201*, 104498. [CrossRef]
38. Pei, X.; Li, Z.; Li, R.; Pei, L.; Liu, C.; Gao, J.; Wei, F.; Wu, S.; Wang, Y.; Chen, Y. LA-ICP-MS U-Pb ages of detrital zircons from the meta-detrital rocks of the Early Palaeozoic Huluhe Group in eastern part of Qilian orogenic belt: Constraints of material source and sedimentary age. *Earth Sci. Front.* **2012**, *19*, 205–224. (In Chinese)
39. Fu, C.; Yan, Z.; Wang, B. Discussion on the age and tectonic affinity of the mafic rocks in Qingshui-Zhangjiachuan of the conjunction area between the Qinling and Qilian orogenic belts. *Acta Petrol. Sin.* **2019**, *35*, 3141–3160. (In Chinese) [CrossRef]
40. He, S.; Wang, H.; Xu, X.; Zhang, H.; Ren, G. Geochemical characteristics and tectonic environment of Hongtubu basalts and Chenjiahe intermediate-acid volcanic rocks in the eastern segment of North Qilian orogenic belt. *Acta Petrol. Et Mineral.* **2007**, *26*, 295–309. (In Chinese)
41. Li, W. Geochronology and Geochemistry of the Ophiolites and Island-Arc-Type Igneous Rocks in the Western Qinling Orogen and the Eastern Kunlun Orogen: Implication for the Evolution of the Tethyan Ocean. Ph.D. Dissertation, University of Science and Technology of China, Hefei, China, 2008. (In Chinese).
42. Lu, S.; Chen, Z.; Li, H.; Hao, G.; Xiang, Z. Two magmatic belts of the Neoproterozoic in the Qinling Orogenic Belt. *Acta Geol. Sin.* **2005**, *79*, 165–173. (In Chinese)
43. Pei, X.; Ding, S.; Zhang, G.; Liu, H.; Li, Z.; Li, W.; Liu, Z.; Meng, Y. Zircons LA-ICP-MS U-Pb dating of Neoproterozoic granitoid gneisses in the North Margin of West Qinling and geological implication. *Acta Geol. Sin.* **2007**, *81*, 772–786. (In Chinese)
44. Yan, Q.; Wang, Z.; Chen, J.; Yan, Z.; Wang, T.; Li, Q.; Jiang, C.; Zhang, Z. Tectonic Setting and SHRIMP Age of Volcanic Rocks in the Xieyuguan and Caotangou Groups: Implications for the North Qinling Orogenic Belt. *Acta Geol. Sin.* **2007**, *81*, 488–500. (In Chinese)
45. Wang, H.; Chen, L.; Sun, Y.; Liu, X.; Xu, X.; Chen, J.; Zhang, H.; Diwu, C. similar to 4.1 Ga xenocrystal zircon from Ordovician volcanic rocks in western part of North Qinling Orogenic Belt. *Chin. Sci. Bull.* **2007**, *52*, 3002–3010. [CrossRef]
46. Wang, J.; Zhang, H.; Xu, W.; Cai, H. Petrogenesis of granites from Dangchuan area in West Qinling Orogenic belt and its tectonic implication. *Earth Sci.-J. China Univ. Geosci.* **2008**, *33*, 474–486. (In Chinese)

47. Pei, X.; Ding, S.; Zhang, G.; Liu, H.; Li, Z.; Li, G.; Liu, Z.; Meng, Y. The LA-ICP-MS zircons U-Pb ages and geochemistry of the Baihua basic igneous complexes in Tianshui area of West Qinling. *Sci. China Ser. D Earth Sci.* **2007**, *50*, 264–276. [CrossRef]
48. Pei, X.; Ding, S.; Hu, B.; Li, Y.; Zhang, G.; Guo, J. Definition of the Guanzizhen ophiolite in Tianshui area, western Qinling, and its geological significance. *Geol. Bull. China* **2004**, *23*, 1202–1208. (In Chinese)
49. Paton, C.; Woodhead, J.D.; Hellstrom, J.C.; Hergt, J.M.; Greig, A.; Maas, R. Improved laser ablation U-Pb zircon geochronology through robust downhole fractionation correction. *Geochem. Geophys. Geosystems* **2010**, *11*, Q0AA06. [CrossRef]
50. Leake, B.E.; Woolley, A.R.; Birch, W.D.; Gilbert, M.C.; Grice, J.D.; Hawthorne, F.C.; Kato, A.; Kisch, H.J.; Krivovichev, V.G.; Linthout, K.; et al. Nomenclature of amphiboles; Report of the subcommittee on Amphiboles of the International Mineralogical Association Commission on New Minerals and Mineral Names. *Eur. J. Mineral.* **1997**, *9*, 623–651. [CrossRef]
51. Xiang, H.; Connolly, J.A.D. GeoPS: An interactive visual computing tool for thermodynamic modelling of phase equilibria. *J. Metamorph. Geol.* **2022**, *40*, 243–255. [CrossRef]
52. Holland, T.J.B.; Powell, R. An improved and extended internally consistent thermodynamic dataset for phases of petrological interest, involving a new equation of state for solids. *J. Metamorph. Geol.* **2011**, *29*, 333–383. [CrossRef]
53. Green, E.C.R.; White, R.W.; Diener, J.F.A.; Powell, R.; Holland, T.J.B.; Palin, R.M. Activity-composition relations for the calculation of partial melting equilibria in metabasic rocks. *J. Metamorph. Geol.* **2016**, *34*, 845–869. [CrossRef]
54. Sun, S.S.; McDonough, W.F. Chemical and isotopic systematics of oceanic basalts: Implications for mantle composition and processes. *Geol. Soc. Lond. Spec. Publ.* **1989**, *42*, 313–345. [CrossRef]
55. White, R.W.; Powell, R. Melt loss and the preservation of granulite facies mineral assemblages. *J. Metamorph. Geol.* **2002**, *20*, 621–632. [CrossRef]
56. Wei, C.; Guan, X.; Dong, J. HT-UHT metamorphism of metabasites and the petrogenesis of TTGs. *Acta Petrol. Sin.* **2017**, *33*, 1381–1404. (In Chinese)
57. Wang, W.-R.; Dunkley, E.; Clarke, G.L.; Daczko, N.R. The evolution of zircon during low-P partial melting of metapelitic rocks: Theoretical predictions and a case study from Mt Stafford, central Australia. *J. Metamorph. Geol.* **2014**, *32*, 791–808. [CrossRef]
58. Kelsey, D.E.; Clark, C.; Hand, M. Thermobarometric modelling of zircon and monazite growth in melt-bearing systems: Examples using model metapelitic and metapsammitic granulites. *J. Metamorph. Geol.* **2008**, *26*, 199–212. [CrossRef]
59. Volante, S.; Blereau, E.; Guitreau, M.; Tedeschi, M.; van Schijndel, V.; Cutts, K. Current applications using key mineral phases in igneous and metamorphic geology: Perspectives for the future. *Geol. Soc. Lond. Spec. Publ.* **2023**, *537*, SP537-2022-254. [CrossRef]
60. Rubatto, D.; Hermann, J.; Buick, I.S. Temperature and Bulk Composition Control on the Growth of Monazite and Zircon During Low-pressure Anatexis (Mount Stafford, Central Australia). *J. Petrol.* **2006**, *47*, 1973–1996. [CrossRef]
61. Rubatto, D.; Chakraborty, S.; Dasgupta, S. Timescales of crustal melting in the Higher Himalayan Crystallines (Sikkim, Eastern Himalaya) inferred from trace element-constrained monazite and zircon chronology. *Contrib. Mineral. Petrol.* **2012**, *165*, 349–372. [CrossRef]
62. Rubatto, D. Zircon: The Metamorphic Mineral. *Rev. Mineral. Geochem.* **2017**, *83*, 261–295. [CrossRef]
63. Kelsey, D.E.; Powell, R. Progress in linking accessory mineral growth and breakdown to major mineral evolution in metamorphic rocks: A thermodynamic approach in the Na_2O-CaO-K_2O-FeO-MgO-Al_2O_3-SiO_2-H_2O-TiO_2-ZrO_2 system. *J. Metamorph. Geol.* **2011**, *29*, 151–166. [CrossRef]
64. Hermann, J.; Rubatto, D. Relating zircon and monazite domains to garnet growth zones: Age and duration of granulite facies metamorphism in the Val Malenco lower crust. *J. Metamorph. Geol.* **2003**, *21*, 833–852. [CrossRef]
65. Flowers, R.M.; Schmitt, A.K.; Grove, M. Decoupling of U–Pb dates from chemical and crystallographic domains in granulite facies zircon. *Chem. Geol.* **2010**, *270*, 20–30. [CrossRef]
66. Reddy, S.M.; Timms, N.E.; Trimby, P.; Kinny, P.D.; Buchan, C.; Blake, K. Crystal-plastic deformation of zircon: A defect in the assumption of chemical robustness. *Geology* **2006**, *34*, 257–260. [CrossRef]
67. Reddy, S.M.; Timms, N.E.; Hamilton, P.J.; Smyth, H.R. Deformation-related microstructures in magmatic zircon and implications for diffusion. *Contrib. Mineral. Petrol.* **2008**, *157*, 231–244. [CrossRef]
68. MacDonald, J.M.; Wheeler, J.; Harley, S.L.; Mariani, E.; Goodenough, K.M.; Crowley, Q.; Tatham, D. Lattice distortion in a zircon population and its effects on trace element mobility and U–Th–Pb isotope systematics: Examples from the Lewisian Gneiss Complex, northwest Scotland. *Contrib. Mineral. Petrol.* **2013**, *166*, 21–41. [CrossRef]
69. Kovaleva, E.; Klötzli, U. NanoSIMS study of seismically deformed zircon: Evidence of Y, Yb, Ce, and P redistribution and resetting of radiogenic Pb. *Am. Mineral.* **2017**, *102*, 1311–1327. [CrossRef]
70. Kovaleva, E.; Klötzli, U.; Habler, G.; Huet, B.; Guan, Y.; Rhede, D. The effect of crystal-plastic deformation on isotope and trace element distribution in zircon: Combined BSE, CL, EBSD, FEG-EMPA and NanoSIMS study. *Chem. Geol.* **2017**, *450*, 183–198. [CrossRef]
71. Dong, J.; Wei, C.; Song, S. Deep subduction and exhumation of micro-continents in the Proto-Tethys realm: Evidence from metamorphism of HP-UHT rocks in the North Qinling Orogen, central China. *Gondwana Res.* **2021**, *104*, 215–235. [CrossRef]
72. Zhang, Q.; Gao, X.; Chen, R.; Zheng, Y. Granulites record the tectonic evolution from collisional thickening to extensional thinning of the Tongbai orogen in central China. *J. Metamorph. Geol.* **2020**, *38*, 265–295. [CrossRef]
73. Currie, C.A.; Hyndman, R.D. The thermal structure of subduction zone back arcs. *J. Geophys. Res.* **2006**, *111*, B08404. [CrossRef]

74. Chen, R.; Zheng, Y. Metamorphic zirconology of continental subduction zones. *J. Asian Earth Sci.* **2017**, *145*, 149–176. [CrossRef]
75. Zhao, S.; Li, S.; Liu, X.; Santosh, M.; Somerville, I.D.; Cao, H.; Yu, S.; Zhang, Z.; Guo, L. The northern boundary of the Proto-Tethys Ocean: Constraints from structural analysis and U–Pb zircon geochronology of the North Qinling Terrane. *J. Asian Earth Sci.* **2015**, *113*, 560–574. [CrossRef]

Disclaimer/Publisher's Note: The statements, opinions and data contained in all publications are solely those of the individual author(s) and contributor(s) and not of MDPI and/or the editor(s). MDPI and/or the editor(s) disclaim responsibility for any injury to people or property resulting from any ideas, methods, instructions or products referred to in the content.